Two-Dimensional Infrared Spectra of the $^{13}C=^{18}O$ Isotopomers of Alanine Residues in an α-Helix

Chong Fang and Robin M. Hochstrasser*

Department of Chemistry, University of Pennsylvania, Philadelphia, Pennsylvania 19104-6323

Received: May 13, 2005; In Final Form: July 21, 2005

The parameters needed to describe the two-dimensional infrared (2D IR) spectra of the isotopically labeled α-helix are presented. The 2D IR spectra in the amide-I′ spectral region of a series of singly $^{13}C=^{18}O$-labeled 25-residue α-helices were measured by three-pulse heterodyned spectral interferometry. The dependence of the spectra on the population time was measured. Individual isotopomer levels (residues 11−14) were clearly identified in 2D IR, downshifted by ∼61 cm^{-1} from the main helical band. By analyzing the line shapes of the $^{13}C=^{18}O$ diagonal peaks that appeared at ∼1571.3 ± 0.8 cm^{-1} for all four labeled samples, we observed wider structural distributions for residues 14 and 11 than those for 12 and 13. A small fast component in the correlation function was used to estimate the dynamics of these distributions. In all cases, the v = 1 → 2 transition showed a more Lorentzian-like line shape and also decayed faster than the v = 0 → 1 transition, indicating that the population relaxation time of the v = 2 state was significantly faster than the v = 1 state. The amide transitions with naturally abundant $^{13}C=^{16}O$ appeared at ∼1594 cm^{-1}, forming very weak and blurred cross-peaks with $^{13}C=^{18}O$ isotopomer modes. The effects of spectral interferences on the coherence time dependence of the detection frequency spectrum were also investigated. The methods of first moments and Wigner analysis were developed to circumvent the interference effects on the weak isotopomer transitions. The structural origin of the distributions for individual isotopomers was proposed to be an effect of nearby lysine residues on the intrahelical hydrogen-bond network.

1. Introduction

Methods are needed that can measure the kinetics of sub-millisecond biological *structure changes* without significantly perturbing the system. A residue-by-residue-based analysis of secondary structures undergoing conformational changes in solutions remains an important challenge for spectroscopy. The new two-dimensional infrared methods (2D IR) offer hope of this goal being accomplished soon.[1−3] Both spatial and time resolution are needed to establish a microscopic basis for such structure changes, and these are precisely the features that are provided by 2D IR.[4−7] At the same time, a strategy of applying infrared methods to complex systems with many overlapping transitions is needed. One approach has involved double-isotope selection where two residues of interest are isotopically selected, one with $^{13}C=^{16}O$ and the other with $^{13}C=^{18}O$. The 2D IR method then can measure the coupling and angular dispositions of the two selected C=O groups.[8,9] Another has involved experiments that incorporate multiple frequencies that can simultaneously access different vibrational states.[10] By means of these approaches, we have recently determined the signs and magnitudes of couplings between various residues in peptides and helices.[9,11] In principle, these methods should be applicable to any protein secondary structure into which isotopically selected residues could be introduced, so it has wide application.

Isotope labeling of a few chemical groups, those key to the events of interest, has chemical bond specificity and is non-perturbative. Isotope editing has enlarged the scope of both coherent nonlinear and conventional vibrational spectroscopy and circular dichroism[12−15] applied to lipids, membranes,

peptides and proteins,[16] and enzyme reaction intermediates,[17] even shifting the IR spectra of whole proteins.[18] Isotope substitution has always been a successful strategy of IR spectroscopy, and the applications to biological systems are a natural development[19] whose use is growing[8,20−28] concomitantly with the wider use of peptide synthesis resources. The amide-I mode is largely a carbonyl stretch, and so its frequency is significantly modified by replacement of ^{12}C by ^{13}C (shift −38 cm^{-1}), ^{16}O by ^{18}O (shift −35 cm^{-1}), both ^{12}C and ^{16}O by ^{13}C and ^{18}O (shift −64 cm^{-1}), and N−H by N−D (approximate shift −1000 cm^{-1}). Any one of these substitutions can permit spectral selection of a particular residue. Of these isotopes only ^{13}C occurs significantly enough in natural abundance (1.1%) to interfere with the spectral selectivity, hence the preferred use of $^{13}C=^{18}O$.[8,9,29] We established by means of 2D IR with *two* selected amides, one with $^{13}C=^{16}O$ and the other with $^{13}C=^{18}O$, that the naturally abundant population makes little or no contribution to the coupling between the two selected groups,[8,9] even in larger systems where the probability of having a ^{13}C substitution in the macromolecule by natural abundance approaches unity. In other recent work, 2D IR spectroscopy with $^{13}C=^{18}O$ isotope labeling has been used to study an amide-I vibrational line shape in a lipid vesicle.[30]

As an extension of the studies of 25-residue α-helices having both $^{13}C=^{16}O$ and $^{13}C=^{18}O$ labels,[9] the present work focuses on single $^{13}C=^{18}O$ labels on the same helix. The significant shift of the $^{13}C=^{18}O$ isotopic label pushes it outside the main helical band of states formed by the unlabeled 24 residues, therefore enabling us to analyze the energetics and dynamics at a residue level without significant effects of excitation exchange between residues.

* Author to whom correspondence should be addressed. Phone: 215-898-8203. Fax: 215-898-0590. E-mail: hochstra@sas.upenn.edu.

2D IR Spectra of Isotopomers of an α-Helix

J. Phys. Chem. B, Vol. 109, No. 39, 2005 **18653**

The objectives of the work include finding a structural basis from 2D IR for any differences in the relaxation dynamics of populations and coherences at individual residues in the helix and the development of processing methods to extract parameters from weak isotopomer transitions in the presence of strong modulations by nearby states of the helix. In particular, we aimed to generate experimentally based descriptions of the distributions of amide frequencies that are associated with different sites and to relate these to structural features. We also sought to expose the dynamics of these distributions and the possible role of the solvent. Another aim was to use the isotopomer results to test further the theoretical idea that helix amide-I states can be considered as deriving from an interacting set of degenerate transitions. Finally, to strengthen the usefulness of the double-isotope strategy,[9] it was important to completely characterize the involvement of the naturally abundant $^{13}C{=}^{16}O$ isotopomer transitions in 2D IR spectra and to lay a basis for future experiments on even less-symmetric secondary structures.

2. Experimental Methods

Sample Preparation. The series of $^{13}C{=}^{18}O$ isotopically labeled 25-residue alanine-rich α-helical polypeptides of the sequence $Ac{-}(A)_4K(A)_4K(A)_4K(A)_4K(A)_4Y{-}NH_2$ were obtained from BioMer Technology. The molecular weight of the synthesized product ($m/z \approx 2159.5$ Da) was verified by mass spectrometry, and the purities of the samples were all higher than 95%. Fmoc-protected $^{13}C{=}^{18}O$-labeled alanine was synthesized in exactly the same way as described previously.[9] The peptide with the $^{13}C{=}^{18}O$ label at residue n (counting from the N-terminus) is referred to as [n], and $n = 0$ when there is no isotopic label in the helix.

To obtain the peptide samples in aqueous solutions for 2D IR measurements, $\sim$2.0 mg of peptide was first dissolved in 0.1% phosphoric acid in 2.0 mL of pure D_2O to allow for complete deuteration of the molecules in an acidic environment, then lyophilized. The final product was resuspended in 100 μL of pure D_2O to a concentration of $\sim$4.5 mM ($\sim$10 mg/mL), having the uncorrected pH value in the range of 2−3. About 3.8 μL of the peptide solutions was then sandwiched by two CaF_2 windows (25 mm diameter, 2 mm thickness, JANOS Technology Inc., Townshend, VT) with a 25 μm Teflon spacer (Harrick Scientific Co., Ossining, NY), but the peptide solution was not in contact with the surrounding spacer to avoid sample evaporation or contamination. The sample cells were temperature-controlled.

Linear-IR Spectroscopy. The Fourier transform IR (FTIR) absorption spectra in the amide-I′ region (the prime indicates the amide-I mode with amide proton deuteration[31]) were recorded on a Perkin-Elmer Spectrum 2000 Explorer FTIR spectrometer with 1.0 cm^{-1} resolution at 0 °C, controlled by a NESLAB RTE-7 Digital One refrigerated bath (Thermo Electron Corporation, Newington, NH). The results are shown in Figure 1. The main helical band of samples [11] to [14] all peak at $\sim$1632 cm^{-1}, while [0] peaks at $\sim$1633 cm^{-1}. The peak absorbance variations from 0.16 to 0.36 OD are due to concentration differences of samples (UV absorbance of residue Y ($\epsilon = 1450$ M^{-1} cm^{-1} at 274 nm) showed that [11] and [14] had relatively higher concentrations than [12] and [13]) and variations in cell path length.

Four Gaussian profiles fit the spectral region 1550−1720 cm^{-1} of the FTIR of all labeled samples: one for the $^{13}C{=}^{18}O$ isotopic label, one for the $^{13}C{=}^{16}O$ natural abundance peak, and two for the unlabeled carbonyl groups. The unlabeled

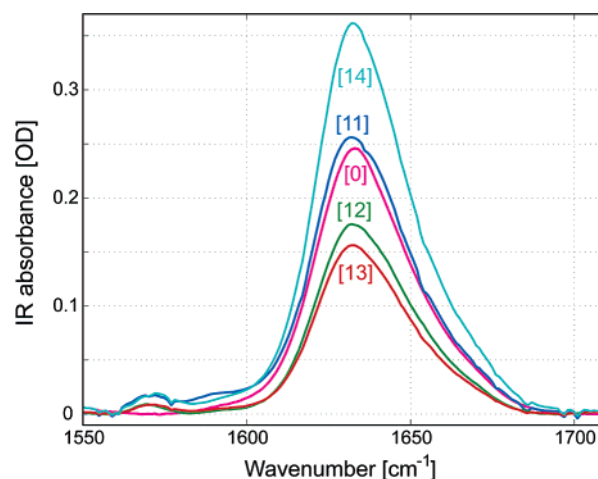**Figure 1.** Linear FTIR spectra of a series of $^{13}C{=}^{18}O$ isotopically labeled α-helices [11], [12], [13], and [14] (notation defined in the text) at 0 °C in the D_2O/0.1% phosphoric acid buffer solution. The unlabeled sample [0] is shown for comparison.

peptide has no significant spectral feature in the region of 1560−1584 cm^{-1}. The two components of the main helical band consist of vibrational transitions from the $^{12}C{=}^{16}O$ groups peaking at $\sim$1631.6 ± 0.2 cm^{-1} with a full width at half-maximum (fwhm) of $\sim$27.3 cm^{-1} and at $\sim$1654.3 ± 0.8 cm^{-1} (fwhm $\sim$32.4 cm^{-1}). They have an intensity ratio of $\sim$2.51 ± 0.08. The former component corresponds to the α-helical polypeptide in aqueous solution, while the weaker higher-frequency component corresponds to the less-ordered structures or frayed ends of the helix.[32]

The peak at $\sim$1594 cm^{-1} is due to $^{13}C{=}^{16}O$ in natural abundance. It has a fwhm of $\sim$21.2 cm^{-1}, which is significantly broader than the $^{13}C{=}^{18}O$ peak (fwhm $\sim$12.2 cm^{-1}). The natural abundance peaks are relatively stronger in [11] and [14] than in [12] and [13] (see Discussion). Due to the unavoidable uncertainties in baseline subtraction needed to obtain the background-free linear-IR profiles, especially in the low-frequency region where solute signal is weakest, the line widths of the isotopomer levels should be considered as *minimum* values. All labeled peptides show the $^{13}C{=}^{18}O$ peaks at about the same frequency (1570.7 ± 0.7 cm^{-1}), among which [12] is at the lowest frequency and [14] is at the highest frequency; the fwhm values of [12] and [13] are smaller than those of [11] and [14]. The amide-II′ peak occurs in the region 1545−1550 cm^{-1}; it is a combination of N−H(D) in-plane bending and C−N stretching of the peptide group.[33] It overlaps with the broad HOD bending mode below 1550 cm^{-1} to result in a shoulder that is hard to identify in the linear-IR spectrum.

FTIR spectra of all five samples were also collected at 22 °C. The essential features remained the same, exhibiting the main helical band, the $^{13}C{=}^{16}O$ natural abundance peak, and the $^{13}C{=}^{18}O$ band, but the line widths of the peaks were all broadened to some extent. The main helical band of all of the samples peaked at $\sim$1636 cm^{-1}, showing a significant blue shift from the 0 °C cases, probably a result of the increase in the portion of the less-ordered structures.[34] The fwhm values of the $^{13}C{=}^{18}O$ peaks in Figure 1 at 0 °C were measured to be 13.0, 11.1, 11.5, and 13.0 cm^{-1} for [11] to [14], respectively.

Two-Dimensional IR Spectroscopy. The 2D IR experiments in the 6 μm region were conducted using three-pulse hetero-dyned spectral interferometry. In this experiment,[2,8,11] three incident infrared pulses on the sample generate a field that is measured by mixing with a fourth pulse on a detector. The detection consisted of a liquid-nitrogen-cooled 64-channel MCT

array detector (MCT-12-64 by InfraRed Associates Inc., Stuart, FL), having elements spaced in the spectrum by ~5.6 nm, and a multichannel laser pulse integrator system (IR-6416 by Infrared Systems Development Corporation, Winter Park, FL). The generated photon echo field with wavevector $\vec{\mathbf{k}}_{PE} = -\vec{\mathbf{k}}_1 + \vec{\mathbf{k}}_2 + \vec{\mathbf{k}}_3$ was collimated with the fourth laser beam ($\vec{\mathbf{k}}_{LO}$), and the combined beams were dispersed by a 120 groove/mm diffraction grating in a monochromator (SPEX by JY Optical Systems Instruments SA, Inc., Edison, NJ) and directly recorded by the array detector. The sensitivity of each element of the array detector was obtained by scanning the monochromator from 5400 to 7300 nm in 10 nm steps and recording the local oscillator pulse spectrum at each position for comparison. After the OPA output frequency was tuned to ~1571 cm^{-1} at the center frequency of the $^{13}C = ^{18}O$ isotopomer mode, all three incoming beam directions and the sample cell position were optimized to obtain the maximal interference strength between $\vec{\mathbf{k}}_{LO}$ and $\vec{\mathbf{k}}_{PE}$. The sample cells were cooled by water circulation and stabilized at 0 °C in the air-purged optical system for at least 45 min before the 2D IR experiments were carried out to ensure that the sample temperature was equilibrated and the outside-sample-cell water absorption in the beam path was excluded. Two pulse sequences were used in the experiments. The sequence with the pulse having wavevector $-\vec{\mathbf{k}}_1$ arriving first gives the rephasing spectrum (R). When pulses $-\vec{\mathbf{k}}_1$ and $\vec{\mathbf{k}}_2$ are interchanged, the nonrephasing spectrum (NR) is obtained. The coherence time interval τ between the first two pulses was scanned in 3-fs steps from −1800 to +2100 fs, by moving the $-\vec{\mathbf{k}}_1$ and $\vec{\mathbf{k}}_2$ translation stages separately for R and NR measurements. The third pulse $\vec{\mathbf{k}}_3$ was scanned in 20-fs steps from 0 to 500 fs to obtain the signal dependence on the waiting (or population) time interval (T) between the second and third pulses (between $\vec{\mathbf{k}}_2$ and $\vec{\mathbf{k}}_3$ in R or between $-\vec{\mathbf{k}}_1$ and $\vec{\mathbf{k}}_3$ in NR). The local oscillator beam was fixed to arrive 1500 fs earlier than the generation of the photon echo induced by $\vec{\mathbf{k}}_3$. In the following text $S_R(\tau,t;T)$ and $S_{NR}(\tau,t;T)$ are the full third-order responses with rephasing and nonrephasing sequences where the time t is the detection time. The spectrum $\tilde{S}(\tau,\omega_t;T)$ with magnitude $|\tilde{S}(\tau,\omega_t;T)|$ is obtained by a partial Fourier transform of the heterodyned photon echo signal along the t axis, and the double Fourier transform yields the complex 2D IR spectrum $S(\omega_\tau,\omega_t;T)$. The real parts of the resulting R and NR complex spectra after proper phase adjustments are then added with the same weight to obtain the 2D correlation (or absorptive) spectra at various waiting times T.

To optimize the signal from the $^{13}C = ^{18}O$-substituted amide-I′ group, the center frequency of the excitation laser pulses was tuned to ~1571 cm^{-1}. Therefore, the 100−120-fs mid-IR pulses that we used did not uniformly span the spectral range from the unlabeled carbonyl groups to the amide-I′ isotopomer levels. The spectral window for 2D IR measurement here was about 1525−1625 cm^{-1}. The amide-I′ modes of the single $^{13}C = ^{18}O$ isotopes in all labeled samples were located in the center of this probing window where the pulse spectrum was flat. In this configuration, the spectra of the unlabeled residues and the amide-II′ mode of the carbonyl groups at lower frequencies are somewhat distorted.

The signal $|\tilde{S}(0,\omega_t;T)|$ corresponds to a spectrally resolved transient grating. It is obtained by setting the coherence time interval τ equal to zero. Pump−probe spectra were collected with the same setup as for the 2D IR correlation measurement, except that the $\vec{\mathbf{k}}_3$ and $\vec{\mathbf{k}}_{LO}$ beams were both blocked and the $\vec{\mathbf{k}}_2$ probe beam intensity was reduced by a factor of ~10 compared with the $\vec{\mathbf{k}}_1$ pump beam. The difference in transmission of the

$\vec{\mathbf{k}}_2$ pulse with and without the $\vec{\mathbf{k}}_1$ pulse pumping the sample was then measured as a function of the time delay between the pump and probe pulses. The difference spectra were subsequently divided by the spectrum of the $\vec{\mathbf{k}}_2$ pulse to generate the time-dependent pump−probe spectra of each sample.

The 2D IR spectra of the four labeled samples and the unlabeled sample were collected within a short period of time under very similar experimental conditions, including physical locations of the translation stages. The detector frequency was calibrated by scanning the monochromator over several strong water absorption peaks. The 2D IR correlation spectra of each sample were collected at least three times to confirm frequency reproducibility, and the average values were given in the following discussion. The frequency precision was ±0.5 cm^{-1} in the 2D IR spectra.

3. Results and Discussion

The theory of the response functions and the signal treatment for 2D IR spectra have been discussed previously,[4−6,11] and it is known that the dependence of the photon echo signal on the population time T is quite different for a set of oscillators than that for a single oscillator because of the modulation in the sum of the fields generated by the oscillators. There are also effects of interference between signals from different modes when there is overlap between those broadened transitions. A simple illustrative model of the type of signal that we are observing consists of two oscillators A and B with the same homogeneous relaxation rate γ for which the signal is

$$S_R(\tau,t;0) = [e^{i\omega_A\tau} e^{-i\omega_A t} + e^{i\omega_B\tau} e^{-i\omega_B t}]e^{-\gamma(\tau+t)} \quad (1)$$

The different signs of the phase accumulation on the τ and t axes cause the occurrence of an echo. A stimulated echo signal $E(\tau)$ from such a response, using pulses whose spectra bracket both resonances, is the magnitude squared of $S_R(\tau,t;0)$ integrated over the detector time t:

$$E(\tau) = e^{-2\gamma\tau}[1/\gamma + 2\cos(\delta\omega_{BA}\tau - \phi_{BA})/(\delta\omega_{BA}^2 + 4\gamma^2)^{1/2}] \quad (2)$$

which oscillates at the frequency $\delta\omega_{BA} = \omega_B - \omega_A$ with phase $\phi_{BA} = \arctan(\delta\omega_{BA}/2\gamma)$. The phases depend on the relaxation times and the frequency separations. The real part of the complex spectrum at the resonance ω_A of this simple response is

$$Re\{\tilde{S}_R(\tau,\omega_A;T)\} = [(e^{-\gamma\tau}/\gamma)(\cos\omega_A\tau + \gamma\cos(\omega_B\tau + \phi_{BA}')/(\gamma^2 + \delta\omega_{BA}^2)^{1/2})] \quad (3)$$

which is a carrier wave at close to ω_A modulated at the difference frequency with phase $\phi_{BA}' = \arctan(\delta\omega_{BA}/\gamma)$. These modulations and the interferences in the absolute magnitude grow larger as the overlap of the two resonances increases. The spectrum $|\tilde{S}_R(\tau,\omega_A;T)|$ also oscillates at the difference frequency due to the interference arising from the cross-terms between the two oscillators in the magnitude squared. When more than two transitions, inhomogeneous broadening, and spectral diffusion are included, these principles are not changed but the peak of the envelope of the echo signal along τ is shifted to positive values of τ, and its position may vary with T. In other words, the interference in the magnitude signal influences the shift of the peak of the echo envelope along the τ axis so that the simple relationships between the conventional echo peak shift and the vibrational frequency correlation functions[35−38] are
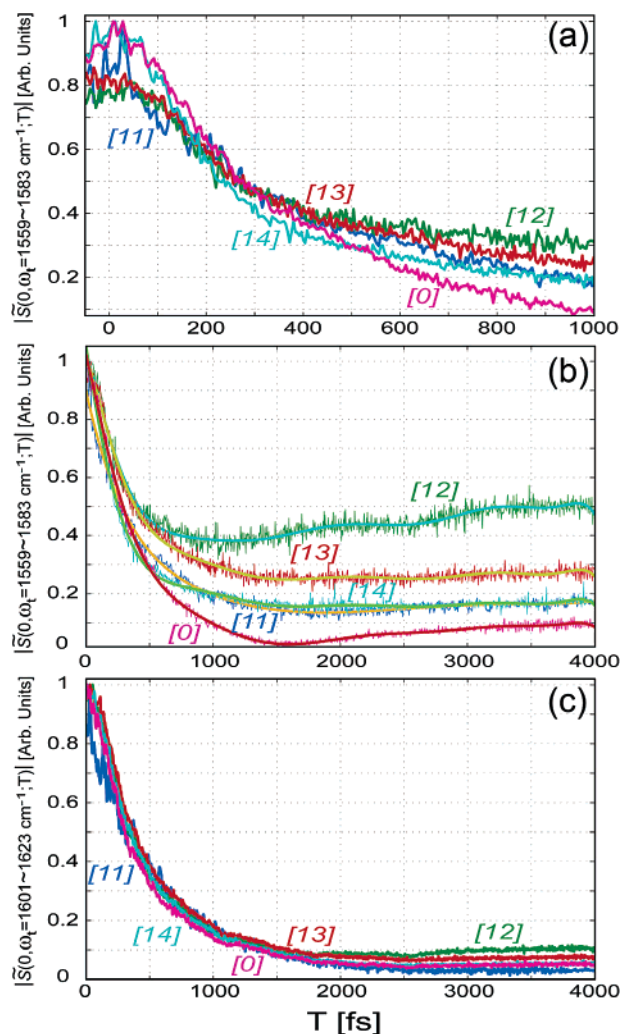
Figure 2. Transient grating data consisting of $|\tilde{S}(0,\omega_t;T)|$: (a) integrated over the detection frequency range of the $^{13}C{=}^{18}O$ transition (1559–1583 cm^{-1}) for the four labeled samples [11], [12], [13], and [14] and the unlabeled sample [0] within a 1-ps time frame; (b) same as part a but for a longer time scale up to 4 ps; (c) for the main helical band region of 1601–1623 cm^{-1}.

no longer valid. These considerations must be dealt with to extract useful properties from 2D IR spectra of amide-I transitions in polypeptides where there are a large number of distributed but overlapping transitions due to different isotopomers.

  Transient Grating and Pump−Probe Results. The transient grating data were analyzed in three characteristic spectral regions corresponding to $^{12}C{=}^{16}O$, $^{13}C{=}^{16}O$, and $^{13}C{=}^{18}O$ isotopomer levels, respectively. The data are shown in Figure 2a for the $^{13}C{=}^{18}O$ isotope region only at short times (<1 ps). All of the samples including [0] showed similar decay curves. The signal in the frequency range of 1601–1623 cm^{-1} (Figure 2c), where the $^{12}C{=}^{16}O$ absorption band of the helix dominated the probing spectral window, gave very similar relaxation times ($\pm5\%$) at delay times prior to 1 ps for all samples. These results showed that the relaxation of these bulk helix states were not significantly perturbed by the insertion of a single $^{13}C{=}^{18}O$ label. There were slight differences between [0] and other samples at later times (>1.5 ps) where all of the samples with one isotopic label exhibited a weak oscillatory signal in the spectral region of $^{13}C{=}^{18}O$ (Figure 2b) that were not present in Figure 2c. The oscillatory signals in samples [11] to [14] most likely arise from modulations between the $^{13}C{=}^{18}O$ transitions and the resonances
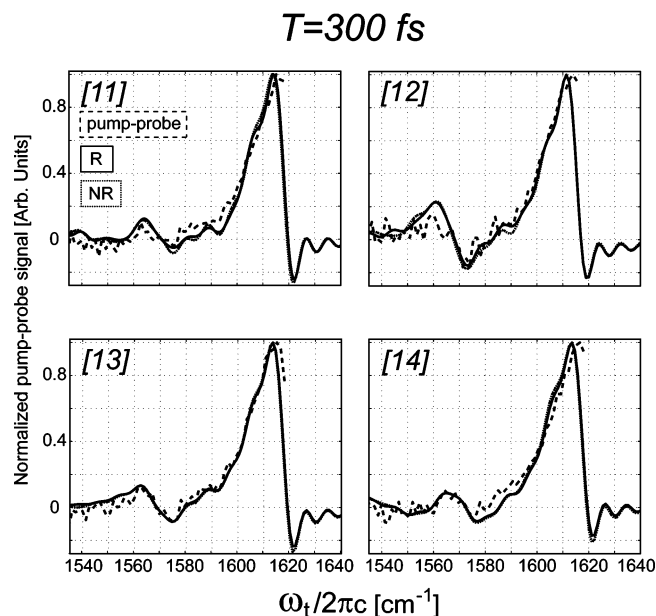

Figure 3. Pump−probe spectra of four labeled samples [11], [12], [13], and [14] (notation defined in the text), shown as dashed lines, compared with the projections of the R and NR spectra onto the ω_t axis, shown as solid and dotted lines, respectively, in the frequency region of interest (1535–1640 cm^{-1}). The waiting time is $T = 300$ fs. The maximum of the main helical band signal is normalized to unity in each case.

from $^{13}C{=}^{16}O$ in natural abundance. The peak separation is ~23 cm^{-1}, which corresponds to an oscillation period in the transient grating along the population time (T) axis of ~1.4 ps in [12], where the modulation was most significant. The tail of the main helical band was also slightly modulated at ~546 fs due to the $^{13}C{=}^{18}O$ isotopic transition separated by a frequency difference of ~61 cm^{-1}. These nonnegligible oscillatory effects as well as the nonzero background caused by the persistent D$_2$O solvent absorption especially at later T times introduced some uncertainty into the relaxation parameters for the $^{13}C{=}^{18}O$ isotopomer levels. The value of $T_1 = 525 \pm 50$ fs was consistent with the transient grating signal decay for all labeled samples, [11] to [14], in the range of Figure 2a. T_1 is the population relaxation time of the $v = 1$ state, and values of T_1 in this range are typical for amide-I modes. After one or two T_1 periods, the initial populations must have relaxed into unknown modes of the helix and solvent that are not considered further in this work.

  The pump−probe spectra at $T = 300$ fs shown in Figure 3 were used to establish phases of the signal and hence the real parts of the R and NR spectra of each labeled sample. The projection of the real part of the 2D IR rephasing spectrum (R) onto the ω_t axis, i.e., Re$\{\int_{band} d\omega_\tau\, \underset{\sim}{S}_R(\omega_\tau,\omega_t;T)\}$, is identically equal to $\tilde{S}(\tau = 0,\omega_t;T)$ when the integration is over all frequencies.[39] This quantity is the pump−probe spectrum. In practice, the integral represents a discrete summation over the bandwidth of the experimental spectrum. The dispersed pump−probe spectra of the helix samples are characterized by three spectral features: the steep change in the low-frequency regime of the main helical band, the frequency separation between the main helical band and the $^{13}C{=}^{18}O$ label, and the line shape in the $^{13}C{=}^{18}O$ isotope region. For the projections of the real part of the 2D IR spectra onto the detection frequency axis, a limited frequency region of 1200–2000 cm^{-1} along the ω_τ axis was selected instead of the whole spectral range to exclude the influence of ringing and noise around the zero frequency regime.
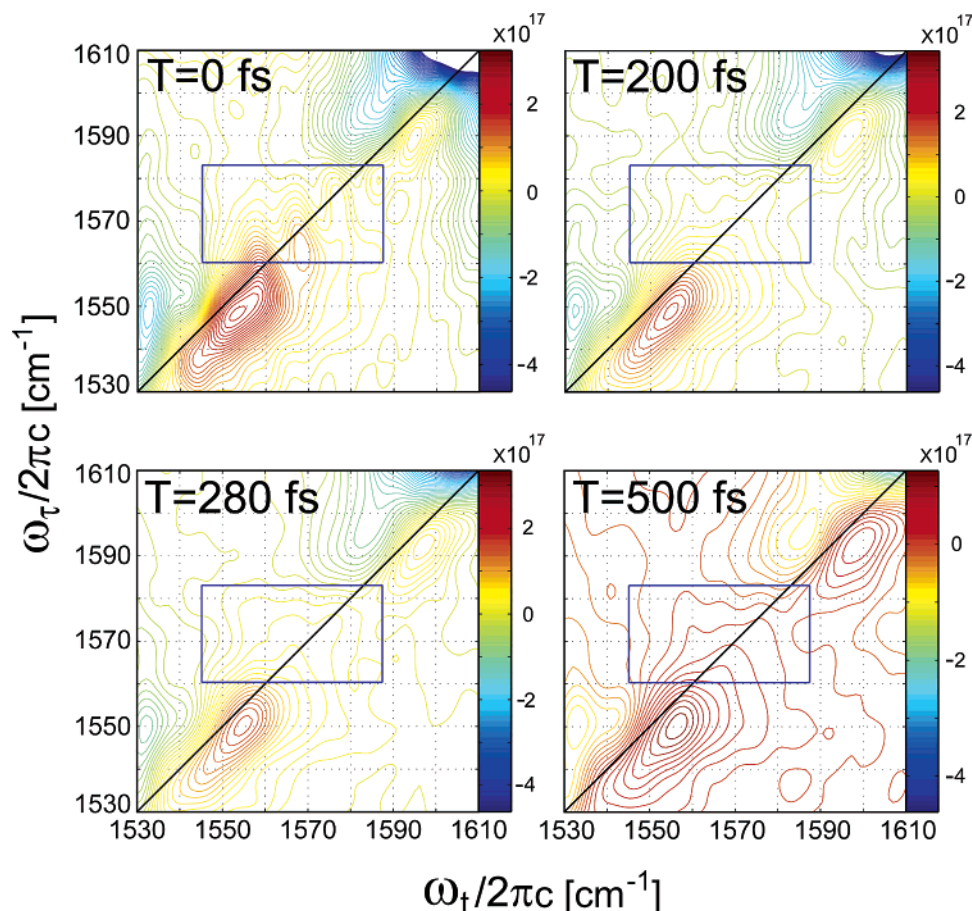
Figure 4. Two-dimensional correlation spectra (real part) of the unlabeled sample [0] at four different values of waiting time ($T = 0$, 200, 280, and 500 fs). The blue rectangular box in each figure highlights the expected frequency region of the $^{13}C=^{18}O$ isotopomer transition.

The spectral region of interest was restricted to be close to the $^{13}C=^{18}O$ isotopomer transition. The 3-mm germanium plates in the beam paths of $-\vec{k}_1$, $\vec{k}_2$, and $\vec{k}_3$ largely compensated for the negative chirp introduced by the 2-mm CaF_2 window in the sample cell. The properly phased R and NR real-part spectra, obtained by matching their respective projected spectra to the pump–probe spectra, were subsequently added in a 1:1 ratio to generate the 2D correlation spectra at various waiting times T.

Two-Dimensional Correlation Spectra Analysis. The 2D correlation spectra of the unlabeled sample [0] at four different values of T from 0 to 500 fs are shown in Figure 4. There is no background signal in the selected $^{13}C=^{18}O$ frequency region, 1560–1583 cm^{-1} along the ω_τ axis and a 43 cm^{-1} span along the ω_t axis, which is marked as a rectangular box in the Figure. From $T = 0$–500 fs, there is no significant spectral change in the selected frequency region, which simplifies the spectral measurements on the four samples [11] to [14]. Each spectrum in Figure 4 clearly shows a transition near 1594 cm^{-1} and an amide-II' transition around 1549 cm^{-1}. The former is attributed to the presence of $^{13}C=^{16}O$ groups from carbon in natural abundance. The shifts are consistent with those seen in helices with added $^{13}C=^{16}O$-substituted residues.[8,25,40,41] Approximately 27.5% of the helices are expected to have at least one residue labeled with a $^{13}C=^{16}O$ group. These groups are presumably randomly distributed along the chain, so the total width of the natural abundance peak gives a qualitative indication of the spread of isotopic shifts, which in turn is related to the heterogeneity of the helix structure.

The correlation spectra of samples [11] to [14] are shown in Figures 5–7 for values of $T = 0$, 300, and 500 fs, with the

$^{13}C=^{18}O$ region again highlighted by the selective frequency box that was defined in Figure 4. The shape of the specific isotopomer transitions appearing as diagonal peaks in the 2D correlation spectra are directly related to the structural and dynamical parameters of the vibrator, namely its spectral diffusion, the diagonal anharmonicity, the frequency correlations, and the differences in dephasing and population decay rates between the $v = 0 \rightarrow 1$ and $v = 1 \rightarrow 2$ transitions.[42]

The signal strength in the natural abundance region was larger for the isotopomers in comparison to [0], which we attribute to $^{13}C=^{16}O$ impurities in the labeled peptides. It is important to establish the effects of coupling of these naturally abundant $^{13}C=^{16}O$ transitions to the $^{13}C=^{18}O$ isotopic label. In our double-isotope 2D IR strategy,[8,9] the coupling between transitions due to specifically labeled $^{13}C=^{16}O$ and $^{13}C=^{18}O$ residues was sought. Therefore any effects of background $^{13}C=^{16}O$ need to be evaluated. Only a fraction of the $^{13}C=^{16}O$-containing naturally occurring helices will have a $^{13}C=^{16}O$-substituted residue sufficiently nearby to the $^{13}C=^{18}O$ label for a significant cross-peak to be formed. The strongest interamide couplings are for nearest ($i, i + 1$) and next-to-nearest neighbors ($i, i + 2$; $i, i + 3$),[9] representing only 6 out of the 25 residues. Such naturally abundant isotopomers are present in only ~7% of the helices. Thus any cross-peak from such effects should have at most 7% of the strength of the cross-peak in the doubly labeled sample. The cross-peaks in the doubly labeled samples are only about 20% of the diagonal peak intensities. This calculation is perfectly consistent with the signals reported here. The observed cross-peaks between the natural abundance peak and the $^{13}C=^{18}O$ mode are overall very weak and difficult to quantify. However, they are more prominent for [12] and [13], which

2D IR Spectra of Isotopomers of an α-Helix

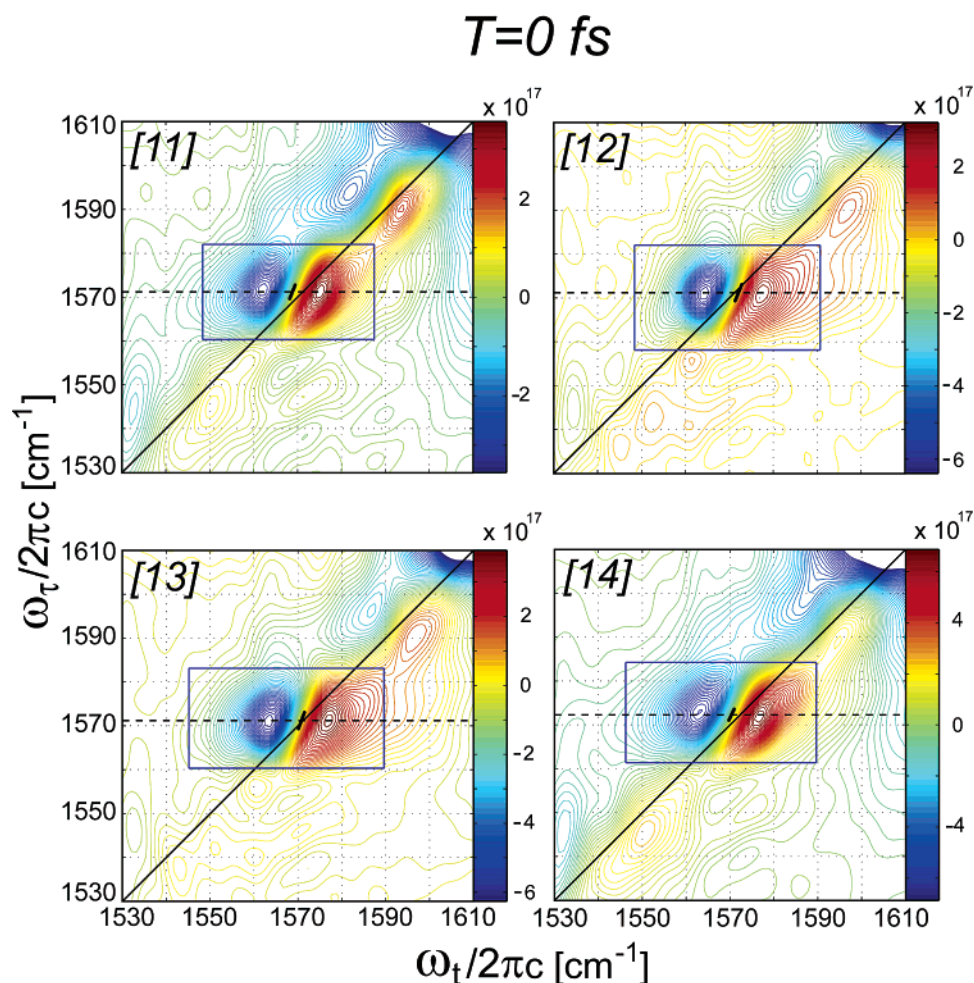*J. Phys. Chem. B, Vol. 109, No. 39, 2005* **18657**

Figure 5. Two-dimensional correlation spectra of the four labeled samples [11], [12], [13], and [14] at zero waiting time ($T = 0$). The black dashed line passes through the center of the vibrational transition peaks of the $^{13}C=^{18}O$ isotopomer level in each sample. The blue rectangular box represents a selected frequency region as in Figure 4, within which the integrated magnitude intensity ratio of Re{R} to Re{NR} is calculated. The zero contour line separating the out-of-phase $v = 0 \rightarrow 1$ and $v = 1 \rightarrow 2$ transition peaks is outlined by the short tilted black bar, from which the slope is measured for each labeled sample.

have the sharpest lines. These cross-peaks are also elongated and blurred along the diagonal, likely due to the randomization of $^{13}C=^{16}O$ natural abundance position within the helical exciton band. This interpretation is confirmed by the results of previous work,[9] showing that there are shifts of the $^{13}C=^{16}O$ transitions due to the presence of $^{13}C=^{18}O$ in nearby residues and that these shifts vary with the separation between residues. According to the present analysis, the coupling peaks between pairs of isotopomer levels ($^{13}C=^{16}O$ and $^{13}C=^{18}O$) in 2D IR are unlikely to be contaminated by the contribution from naturally abundant isotopomers. In our effort to focus this paper on the $^{13}C=^{18}O$ region of the spectrum, the figures do not show the coupling of the $^{13}C=^{16}O$ resonances to the main helical band (at $\omega_\tau \approx 1610-1650$ cm^{-1} and $\omega_t \approx 1580-1610$ cm^{-1}) that was discussed in our previous papers.[8,9]

In regard to the $^{13}C=^{18}O$ diagonal 2D IR spectra in the selected boxes of Figures 5–7, there are always two contributions, one from $v = 0 \rightarrow 1$ and the other from $v = 1 \rightarrow 2$ transitions. These components have opposite signs and are separated by the diagonal anharmonicity of the amide-I′ mode, whose mean is about 9.7 cm^{-1} for the four $^{13}C=^{18}O$ isotopomer levels as listed in Table 1. This value was obtained by fitting the projection onto ω_t of the absorptive spectrum at $T = 300$ fs to two Gaussian profiles representing the $v = 0 \rightarrow 1$ and $v = 1 \rightarrow 2$ transitions. The widths of the Gaussians were constrained

by the dynamical parameters determined by the linear spectrum and the T_1 measurement (transient grating). Naturally the fit is not perfect at the highest and lowest frequencies where the Lorentzian portions dominate. We also fit the projection by two Lorentzians and by two Voigt profiles. In every case, the diagonal anharmonicity was in the similar range of 9.7 ± 1.7 cm^{-1}. None of these choices is an exact representation of the dynamics of the $^{13}C=^{18}O$ isotopomer level because of spectral diffusion.

The figures also show that signal from the $v = 1 \rightarrow 2$ region of the correlation spectrum decays faster than the $v = 0 \rightarrow 1$ part and has a noticeably more Lorentzian line shape. Both of these factors, which are made quantitative by the data analysis and the resulting parameters in Table 1, indicate that the population relaxation rate of the $v = 2$ state is significantly larger than that of the $v = 1$ state of the isotope. For example, the ratio of the $v = 1 \rightarrow 2$ to the $v = 0 \rightarrow 1$ transition line widths along ω_t is ~1.17 ± 0.05 for all of the $^{13}C=^{18}O$ isotopomer transitions. As a result of these differences, the $v = 0 \rightarrow 1$ component is more tilted along the diagonal of the 2D IR correlation spectrum and has an asymmetric shape that is narrower at the lower frequency side. The $v = 1 \rightarrow 2$ component presents a more upright peak than the $v = 0 \rightarrow 1$ component. The $v = 1 \rightarrow 2$ width along the ω_t axis is larger than that of the $v = 0 \rightarrow 1$ transition in all of the samples, while the $v = 1 \rightarrow$
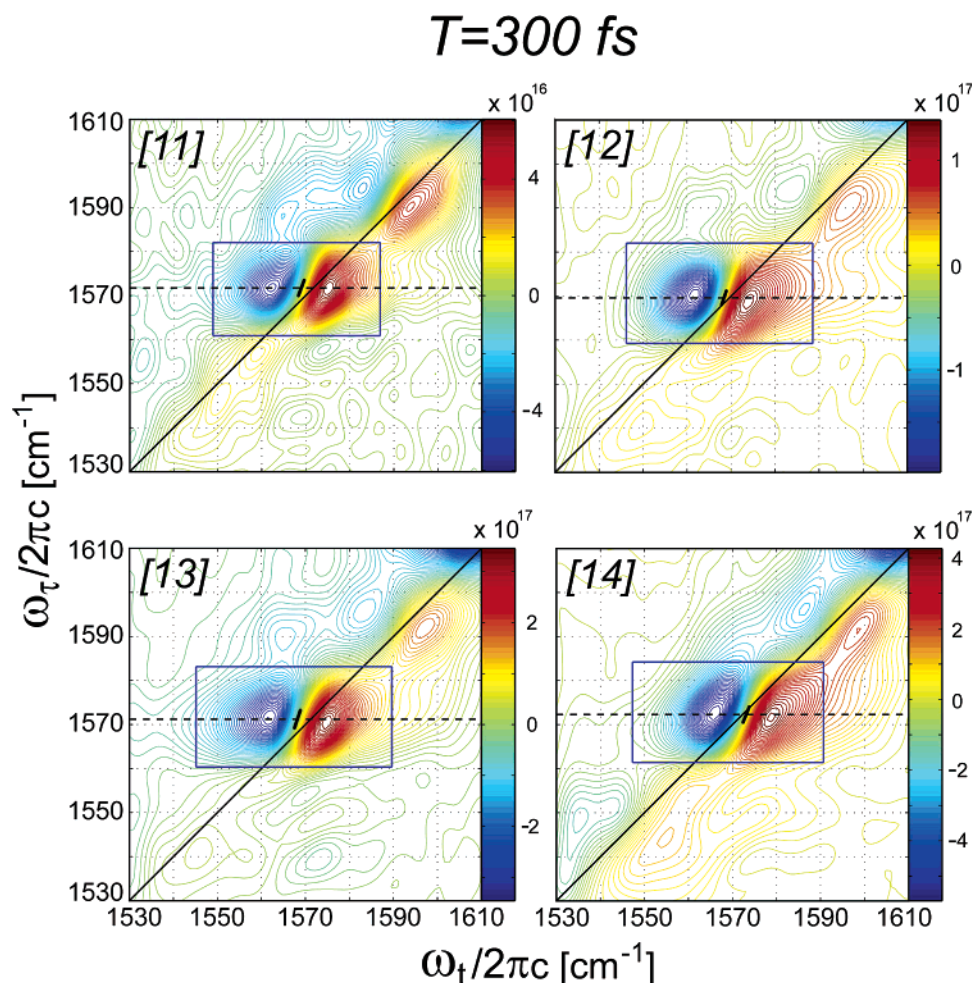
Figure 6. Two-dimensional correlation spectra of the four labeled samples [11], [12], [13], and [14] at $T = 300$ fs (details in Figure 5 caption).

2 width along ω_τ axis is smaller than that for the v = 0 → 1 transition. These features are signatures of the dynamical parameters for all four $^{13}C={}^{18}O$ isotopomers.

To effectively analyze and compare the complex response determining the diagonal peaks of each individual isotopic label in samples [11] to [14], we used a number of different approaches, all of which led to the same basic conclusions regarding the variations of the nonlinear responses at different residues. The data were shown in Table 1. First the slope of the zero contour line separating the out-of-phase v = 0 → 1 and v = 1 → 2 transition regions of the 2D IR spectra was measured. Another parameter that we chose to represent the properties of the isotopomer mode was the ratio of the magnitudes of the Re{R} to the Re{NR}, frequency integrated inside the selected box. This ratio would be unity if the integration had been over the complete frequency range, but it was normally larger than unity when the limited frequency box was selected because of the different line-narrowing properties in the R and NR spectra and the nonzero inhomogeneity of the vibrator.[5,6,9] As predicted by theory and verified by our simulations, a vibrator with larger inhomogeneity will exhibit 2D IR spectra that are elongated more along the diagonal; therefore the slope is reduced, and the frequency-limited ratio becomes larger. For the three typical T values ($T = 0$, 300, and 500 fs) examined in detail here, both the slope and the ratio data consistently suggest that samples [14] and [11] possess significantly larger inhomogeneities than those of [12] and [13], with [14] having the largest and [13] the smallest inhomogeneous distribution. Also the $^{13}C={}^{18}O$ peak positions along

ω_τ are compared, showing the average values for the four labeled samples [11] to [14]: 1571.4, 1570.3, 1571.0, and 1572.3 cm^{-1}, respectively. These results are consistent with those from linear-IR spectra. It is evident that there is a correlation between the amide-I′ vibrational frequency and the inhomogeneous line width of the isotopomer level.

Zero-Order Frequencies. The zero-order isotope shift of ~64 cm^{-1} for $^{13}C={}^{18}O$ is significantly larger than the couplings between residues in the helix,[9,29] so perturbation theory will give an excellent estimate of the repositioning of the energy levels of such an isotopomer due to coupling. The second-order perturbation energy change $\Delta\epsilon_i^{(2)}$ of the isotopic site i is given by $\Delta\epsilon_i^{(2)} = -\delta_i - 2B^2/\delta_i$, where δ_i is the magnitude of the isotope downshift at site i. The isotope shift is considered to be 64 cm^{-1}, consistent with computations.[29] The shift $\Delta\epsilon_i^{(2)}$ depends on the factor $B^2 = \sum_{m\neq i}\beta_{im}^2$, which is the sum of the coupling constants ranging over all of the sites that exist for the particular substitution and helix length. Previously, we obtained a value of $B^2 \approx 117$ (cm^{-1})^2 for sites in the middle region of the helix.[42] This value leads to a shift of $-2B^2/\delta_i \approx -3.7$ cm^{-1} that is considered site-independent. In the present case, all of the isotopomer sites are more than 11 residues from the termini, so the fact that they all appear at almost the same frequency (±1.0 cm^{-1}) indicates that their zero-order frequencies, in the absence of any coupling, are equal within a variance of ±1.0 cm^{-1}. This confirms that the distribution of zero-order energies among the helical amide units is indeed very narrow and that a Hamiltonian matrix with equal diagonal elements is
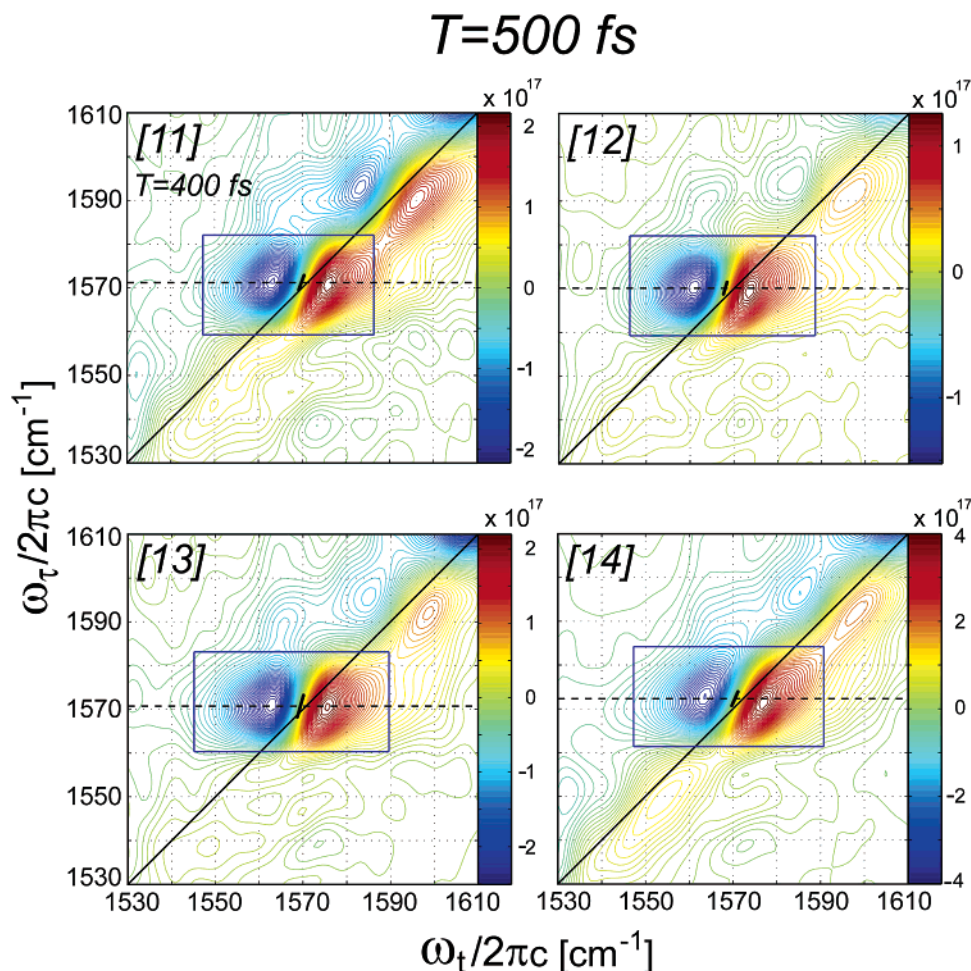
Figure 7. Two-dimensional correlation spectra of the four labeled samples [11], [12], [13], and [14] at $T = 500$ fs (details in Figure 5 caption).

TABLE 1: Comparison of Experimental Properties of α-Helical Isotopomers at 0 °C[a]

	[11]	[12]	[13]	[14]
diagonal anharmonicity[b] (± 1.7 cm^{-1})	10.0	9.9	9.3	9.7
v $= 0 \rightarrow 1$ width along ω_t [b] (± 0.5 cm^{-1})	12.8	11.5	12.2	12.5
v $= 0 \rightarrow 1$ width along ω_τ [c] (± 0.5 cm^{-1})	13.5	14.1	14.0	14.1
v $= 1 \rightarrow 2$ width along ω_t [b] (± 0.5 cm^{-1})	14.7	13.6	14.5	15.0
v $= 1 \rightarrow 2$ width along ω_τ [c] (± 0.5 cm^{-1})	12.8	13.8	14.0	14.4
$S_{1 \rightarrow 2}/S_{0 \rightarrow 1}$ [d] (± 0.05)	1.16	1.15	1.22	1.15
SZ[e] (± 0.05)	2.69	2.96	3.04	2.54
R/NR ratio[f] (± 0.04)	2.04	1.70	1.68	2.22
SZ @ $T = 0$ fs (± 0.05)	2.41	2.54	2.82	2.16
SZ @ $T = 500$ fs (± 0.05)	2.75 ($T = 400$ fs)	3.32	3.53	2.28
R/NR ratio @ $T = 0$ fs (± 0.04)	1.93	1.64	1.57	1.94
R/NR ratio @ $T = 500$ fs (± 0.04)	2.15 ($T = 400$ fs)	1.54	1.61	2.21

[a] Unless otherwise stated, $T = 300$ fs. The estimated standard deviation (σ) for each set of experimental parameters of ^{13}C$=^{18}$O isotopomer transitions is enclosed in parentheses in the first column of the table. [b] Slices through the ^{13}C$=^{18}$O isotopomer peak were averaged over a 12.0 cm^{-1} fwhm Gaussian profile along the ω_τ axis and centered at the peak. Values of the peak width (fwhm) and the diagonal anharmonicity were obtained by Gaussians, Lorentzians, or Voigt profile curve fitting of the crossing region of the v $= 0 \rightarrow 1$ and v $= 1 \rightarrow 2$ spectral components as discussed in the text. [c] Slices through the peak were averaged over a 1.0 cm^{-1} fwhm Gaussian profile along the ω_t axis and centered at the peak. The fwhm values were obtained by Gaussian or Lorentzian curve fitting of the center region of either the v $= 0 \rightarrow 1$ or the v $= 1 \rightarrow 2$ spectral component. [d] The ratio of the v $= 1 \rightarrow 2$ to the v $= 0 \rightarrow 1$ transition line widths is reported as the average value of results from various curve-fitting procedures (Gaussian−Gaussian, Gaussian−Lorentzian, and Lorentzian−Lorentzian) along the ω_t axis from the 2D correlation spectrum of each isotopomer level. [e] SZ is the slope of the zero contour line separating the out-of-phase v $= 0 \rightarrow 1$ and v $= 1 \rightarrow 2$ diagonal transition peaks in the 2D correlation spectrum. [f] The ratio of the magnitudes of the Re{R} to the Re{NR} echo responses is integrated over the frequency region of 1560−1583 cm^{-1} along the ω_τ axis and a 43 ± 1 cm^{-1} span along the ω_t axis that brackets most of the ^{13}C$=^{18}$O isotopomer transitions in the 2D correlation spectrum of each labeled sample.

a reasonable description of helix vibrational states.[43] The location of the unperturbed energy of the helix band of states is obtained by adding $\Delta\epsilon_i^{(2)}$ to the observed vibrational frequency of the isotopomer level. This process yields values within

1 cm^{-1} of 1639 cm^{-1}. The corresponding absorption peak in FTIR measurements is located at ∼1631.6 cm^{-1}. Therefore, we have shown experimentally that the strongly allowed transitions of the α-helix are lowered by ∼7 cm^{-1} by the interresidue
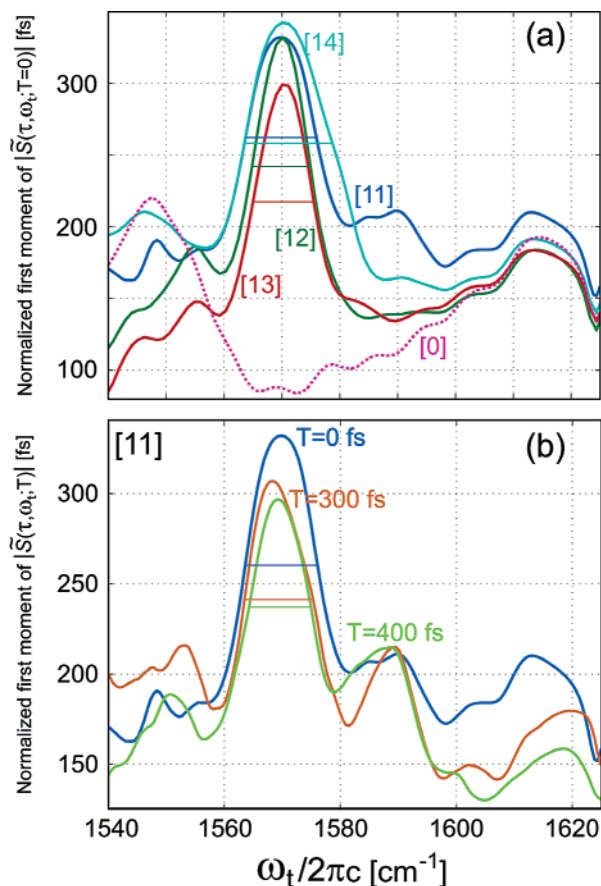
Figure 8. Variation of the normalized first moment along τ of (a) the signal $|\tilde{S}(\tau,\omega_t;T=0)|$ with detection frequency (ω_t) in the region 1540–1625 cm^{-1} for all isotopomers and [0]; (b) the signal $|\tilde{S}(\tau,\omega_t;T)|$ of isotopomer [11] in the same detection frequency range as in part a for $T = 0$, 300, and 400 fs. The four labeled samples have different fwhm values (colored horizontal bars) for their ^{13}C=^{18}O isotopomer transitions. The fwhm values are also shown for each T.

interactions. This result supports the theory[42] that predicts the strong A-state of the α-helix to be downshifted from the zero-order diagonal frequency by ∼10 cm^{-1}.

Normalized First Moment of $|\tilde{S}(\tau,\omega_t;T)|$. The experiments all involve observations of a weak transition near strong transitions. The T dependence of the signal contains information about the correlation function of the frequency fluctuations that are determined by the hydrogen-bond dynamics and structure fluctuations. The modulation by nearby overlapping transitions makes it challenging to extract accurate dynamical parameters for these weak transitions.[44] One approach is to calculate the normalized first moment $M_1(\omega_t;T)$ along τ of $|\tilde{S}(\tau,\omega_t;T)|$:

$$M_1(\omega_t;T) = \int_{-\infty}^{+\infty} \tau|\tilde{S}(\tau,\omega_t;T)|\,d\tau \Big/ \int_{-\infty}^{+\infty} |\tilde{S}(\tau,\omega_t;T)|\,d\tau \quad (4)$$

This property is a measure of the asymmetry of the echo signal along the τ axis.[36] The phase of the modulation by nearby transitions is such that it pushes the main $|\tilde{S}(\tau,\omega_t;T)|$ signal peak away from $\tau = 0$ fs toward larger values. This effect of modulation makes the peak shift itself a poor indicator of inhomogeneity. The first moments were measured and compared with simulations. A comparison of the normalized first moment versus ω_t at $T = 0$ for all of the samples is shown in Figure 8a. This dispersed first moment is a novel representation of the photon echo signals.

It follows directly from the conventional response functions for even a single resonance, such as that in eq 1 averaged over

a distribution of frequencies, that the functional form of $\tilde{S}(\tau,\omega_t;T)$ can be written in a form $A(\tau,T)B(\omega_t,T)$ only when the inhomogeneous distribution vanishes. This statement is valid for the response functions in both the rephasing and the nonrephasing domains and implies that the first moment along τ is independent of ω_t. Otherwise each choice of ω_t generates a function having a different first moment along τ. The signal $\tilde{S}(\tau,\omega_t;T)$ along ω_t and its dispersed first moment along τ both peak at the resonant frequency and have finite widths that vary with the inhomogeneous distribution width. Furthermore, if the frequency correlation function has a finite time evolution, then the shape of the signal along τ, at each value of ω_t, and the first moment change with T in such a way as to narrow as T increases, as is illustrated by the experimental data in Figure 8b. In that case, for a single resonance at frequency ω_A, the signal $\tilde{S}(\tau,\omega_t;T)$ is readily shown by standard methods[5] to be given by

$$\tilde{S}(\tau,\omega_t;T) = e^{i\omega_A\tau-(\tau+2T)/2T_1}\int_0^{\infty} dt\, e^{i\delta t}\, e^{G(\tau,t;T)-t/2T_1} \quad (5)$$

where $\delta = \omega_t - \omega_A$ is the detuning of detection frequency ω_t from the resonance at ω_A and $G(\tau,t;T)$ is the sum of the line shape functions for either rephasing or nonrephasing regimes given by Mukamel.[45]

The [0] sample shows peaks at the amide-II′ transition (∼1548 cm^{-1}), the natural abundance amide-I′ transition, and the helical amide-I′ region, but it has no peak in the ^{13}C=^{18}O amide-I′ region. Samples [11] to [14] show in addition strong peaks due to ^{13}C=^{18}O transitions between 1560 and 1584 cm^{-1}. The full widths at half-maximum (fwhm) of these prominent ^{13}C=^{18}O first moment peaks were 12.3, 10.1, 10.5, and 15.2 cm^{-1} for samples [11] to [14], respectively, so they manifest a similar trend as exhibited by the line widths of the linear-IR measurements. The physical meaning of the fwhm values is that the peak areas in Figure 8 are direct measures of the asymmetry of the echo signal about $\tau = 0$ for these vibrational transitions.[46] The asymmetry is caused by the distributions of vibrational frequencies at the measured sites.

Early Time Dynamics. The ^{13}C=^{18}O peaks in the frequency-dispersed first moment plot (Figure 8a) decayed and narrowed with increasing T because of averaging of the isotopomer frequency distributions. A simple simulation with one inhomogeneously broadened vibrator confirmed that the magnitude of the dispersed first moment was approximately proportional to its width, and both were proportional to the inhomogeneous width. The experimental dispersed first moment plots at the ^{13}C=^{18}O position decayed and narrowed, indicating that spectral diffusion is occurring. One example is shown in Figure 8b for isotopomer [11] for T ranging from 0 to 400 fs. These changes in widths of the dispersed first moment spectra are another manifestation of the tilting of the 2D IR correlation spectra along ω_t as shown in Figures 5–7. The initially excited distribution clearly underwent spectral diffusion, or homogenization, over the first few hundred femtoseconds of the population time delay T. The amide-I′ peak of the main helical band showed a similar trend. However the natural abundance peak showed no such systematic change as T increased, probably because the peak was made up of a static inhomogeneous distribution of isotopomers. The unlabeled compound [0] again served as a useful reference to show that no significant changes occurred with waiting time T in the ^{13}C=^{18}O frequency region. The early time dynamics of the first moment data correspond to only a slight decrease in the asymmetry of the photon echo signal with respect to $\tau = 0$. This result is a manifestation of the rigidity of the polypeptide backbone.[46]
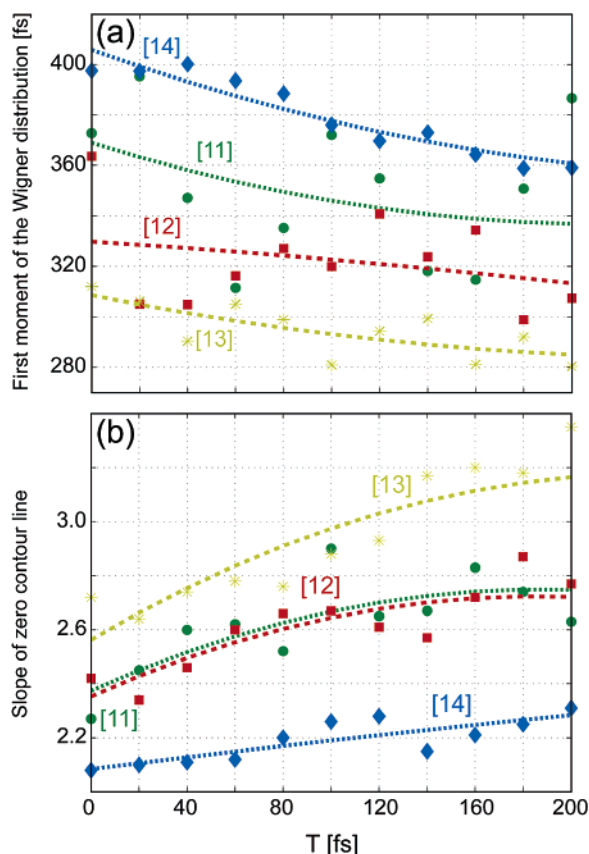
Figure 9. The waiting time (*T*) dependence of two representative dynamic parameters for labeled samples [11], [12], [13], and [14]. The upper illustration (a) shows the first moment of the frequency integrated Wigner spectrum (as defined in the text) in the $^{13}C={}^{18}O$ isotopomer region, decaying with *T* up to 200 fs at 20 fs steps. The lower illustration (b) shows the slope of the zero contour line separating the out-of-phase v = 0 → 1 and v = 1 → 2 $^{13}C={}^{18}O$ diagonal transition peaks in the 2D correlation spectrum varying with *T*. Dashed lines are drawn as a guide through each set of data points.

The Wigner distribution

$$W(\tau,\omega;T) = \int_{-\infty}^{+\infty} \text{Re}\{\tilde{S}(\tau - t/2,\omega_t = \omega_{13C={}^{18}O};T)\} \times$$
$$\text{Re}\{\tilde{S}(\tau + t/2,\omega_t = \omega_{13C={}^{18}O};T)\} \, e^{-i\omega t} \, dt \quad (6)$$

of the oscillatory trajectory at the isotopomer frequency, incorporating both the R and the NR regimes, was also examined. The Wigner distribution of the signal trajectory represents the given signal in terms of time and frequency. It offers a way to examine the time evolution along τ free from the modulations present in a single time trace, which are transformed into their separate frequency components in the Wigner distribution. Each of the frequency components has its characteristic time dependence. The delay of the peak signal from $\tau = 0$ is a measure of the inhomogeneity of the transition. To obtain an averaged parameter, the normalized first moment of $W(\tau,\omega;T)$ was integrated over the frequency (ω) region 1560–1584 cm^{-1} of the $^{13}C={}^{18}O$ isotopomer transition and plotted for various *T* values from 0 to 200 fs at 20-fs intervals as shown in Figure 9a. The results confirm that samples [14] and [11] have larger inhomogeneities than those of [12] and [13]. Furthermore, although difficult to quantify because of interference, there is a small fast component in the decays shown in Figure 9a, indicating that some spectral diffusion is occurring on the 200-fs time scale, consistent with the results from the

dispersed first moment of the echo signal versus *T* data (Figure 8b). These early time characteristics also show up in the 2D IR correlation spectra as variations in the tilt of the v = 0 → 1 transition echo. The tilt is measured from the slope of the zero contour line in 2D IR as indicated by short black bars in Figures 5–7, with their *T* dependences illustrated in Figure 9b and recorded in Table 1. In particular, the slope at *T* = 0 decreases in the order [13], [12], [11], and [14]. Again, the interferences make it difficult to draw quantitative conclusions, but the results indicate the presence of spectral diffusion.

A simulation with a single vibrator representing the $^{13}C={}^{18}O$ isotopomer level was carried out to verify these structural and dynamical inferences. It was found that by choosing a more Gaussian profile for the v = 0 → 1 and a more Lorentzian profile for the v = 1 → 2 component the unique line shapes of samples [11], [12], and [13] displayed in Figure 6 at *T* = 300 fs were reproduced. This parametrization accommodates the fact that the v = 2 state has a significantly faster T_1 than that of the v = 1 state. To generate the slightly different line shape of [14] where the frequency distributions appeared significantly wider, a relatively larger inhomogeneous contribution was needed to simulate its v = 1 → 2 component.

Structural Basis for the Echo Responses. The effects of sequence on secondary structural constraints were sought from the Protein Data Bank (PDB)[47] by examining several proteins having the AAAAK sequence. The cationic lysine residue (Lys) with its side chain tending to be surface-exposed[48] interacts with its neighboring residues through main-chain hydrogen bonding, covalent bonds, and also specific side chain–side chain interactions.[49] It appears that bonding to Lys affects the geometry of the adjacent alanine residues. For instance, the Ala in the Lys–Ala or Ala–Lys sequences adopts a more stretched confirmation in 1WFB.[50] The Lys disturbs the intrahelical hydrogen bond while shortening the Ala carbonyl bond length, hence inducing an increase of the force constant of the carbonyl bond. These structural changes should increase the amide-I vibrational frequency.[51] The atomic coordinates of 1WFB reported in PDB structures indicate that when Ala is hydrogen-bonded to Lys the Ala is structurally altered and the dihedral angles are modified. When the O atom of Ala (residue *i*) hydrogen-bonds to the H atom of Lys (*i* + 4), the torsional angle ψ of Ala is increased; the N–H of Ala bonds to the O atom of Lys (*i* − 4) upstream causing the torsional angle ϕ of Ala to adopt a larger absolute value. A similar structural change of Ala also occurs when it is hydrogen-bonded to other residues with charged side chains, e.g., in 1JQG[52] and 1IYO[53] structures. Therefore the so-called shielding effect is not necessarily a local effect.[54,55] In the sequence studied here, the alanines 11 and 14 are K_{15} − 4 and K_{10} + 4, respectively. This suggests that residues 11 and 14 are hydrogen-bonded both to K and A. However residues 12 and 13 are hydrogen-bonded only to other alanines. Therefore the larger distribution of 11 and 14 frequencies very likely arises from the range of structures deriving from the influence of the lysine residues on their intrahelical hydrogen bonds. The introduction of charged or highly soluble polar residues into the peptide sequence mainly affects the hydration of the C=O and N–H groups of alanine-based polypeptides by forcing the polar groups to interact more weakly with the solvent and more strongly among themselves, leading to the net formation of internal hydrogen bonds.[56] The alanines 12 and 13 have a narrower distribution of frequencies because the ideal helical structure is less perturbed at their sites. These "ideal helix" sites are expected to have more solvent exposure, which is consistent with their relatively lower vibrational frequency.[22] We propose

that this is the primary structural origin of the differences between the vibrational frequency distributions of the four labeled samples.

There are few reports on the sequence dependence of structure by IR spectra that can be compared with the present work. Decatur and co-workers[22] have suggested on the basis of spectral shifts of ^{13}C isotopically substituted residues that the Ala that is $i - 4$ in the sequence from Lys is more shielded from solvent, so it is shifted to a higher frequency. We also invoke Lys, Lys $- 4$ interactions. The ^{13}C=^{18}O isotope 49-Leu studied by Zanni and co-workers[30] in a transmembrane helix by 2D IR represents an important advance but a very different situation from those reported here for helices in aqueous solution. However comparisons between these results will be very interesting to make as more data become available in both environments. Although there have been numerous reports on IR spectra of isotopically replaced residues in α-helices,[23,25,41] to the best of our knowledge the present work along with our previous reports on doubly isotopically substituted α-helices in water[8,9] are the only reported systematic studies of the residue dependence of dynamic parameters of the alanine amide-I transitions in aqueous α-helices.

4. Conclusions

A series of singly ^{13}C=^{18}O-labeled 25-residue α-helical polypeptides were studied by 2D IR three-pulse heterodyned interferometry and other related nonlinear infrared measurements including transient grating and pump−probe spectroscopy. The local environment associated with the helical confirmations was sensed by the individual isotopic labels positioned respectively at residue numbers 11 to 14 on the middle of the helical chain. Insights about the structural and dynamical constraints of the system were then obtained by analyzing the spectral properties in the amide-I′ region stretched into three dimensions (ω_τ, ω_t, and T).

Transient grating data showed that the various ^{13}C=^{18}O isotopomer level v = 1 populations decayed with T at very similar rates. The isotopomer transitions were strongly modulated by the main helical band in the $|\tilde{S}(\tau,\omega_t;T)|$ data. Several useful techniques such as the normalized first moment and a Wigner distribution treatment were adopted that suppress the interference and successfully retrieve the embedded contributions to the vibrational dynamics at the single isotopic site.

Two-dimensional experiments on an unlabeled sample [0] were carried out to serve as the signal background for all of the isotopomer observations. By studying the 2D correlation spectra of the four labeled samples, we found that the 2D IR diagonal peaks had different line shapes: Both had Voigt profiles, but one (v = 1 → 2) was much more Lorentzian-like than the other (v = 0 → 1), indicating the significantly faster population relaxation rate of the v = 2 state than that of the v = 1 state. Simulations of a two-level vibrator representing the ^{13}C=^{18}O isotopomer mode were consistent with these conclusions.

The inhomogeneous contribution manifested itself in 2D IR through the elongation of the diagonal peaks along the diagonal, the slope of the zero contour line between the v = 0 → 1 and v = 1 → 2 transitions, and the antidiagonal line width. There were consistent differences between the observed 2D IR line shapes of various isotopomer levels. Several processing techniques all indicated that [14] and [11] possessed larger inhomogeneities than those of [12] and [13] at the isotopic site. The dynamics in the first several hundred femtoseconds showed a small fast decay component that we attribute to the fluctuations of the amide frequency by the hydrogen bonding to the solvent.

The present data are not complete enough to allow an accurate correlation function to be obtained.

The frequencies of the isotopomer transitions are equal to within about ±1.0 cm^{-1}. This is an important observation that confirms the validity of theoretical approaches that construct the helix states from a set of interacting, mainly degenerate amide transition frequencies.

The natural abundance peaks show up at about the same frequency in all five samples including [0], and they form only very weak cross-peaks with the ^{13}C=^{18}O isotopomer levels in the four labeled samples. These cross-peaks are broad and blurred due to the randomization of ^{13}C=^{16}O natural abundance position within the helical exciton band, which validates our former strategy to use ^{13}C=^{16}O and ^{13}C=^{18}O double isotopic substitution to study the couplings between specific pairs of residues in the helix.

On the basis of several PDB structures and previous work on shielding or helix-stabilization effects by the lysine residue, we conclude that the lysines significantly alter the conformational preferences of those alanines adjacent or hydrogen-bonded to them. Residues 14 and 11 are different from 12 and 13 largely due to the modifications of the intrahelical hydrogen-bond network involving the nearby lysine residues.

This particular set of 2D IR experiments on singly ^{13}C=^{18}O-labeled α-helices provides essential quantitative information about the isotopomer levels in an important secondary structural motif. It identifies the subtle differences between residue-level vibrational transitions and their spectral diffusion. This study lays a basis for future experiments on even less-symmetric secondary structures in both hydrophobic and hydrophilic environments.

References and Notes

(1) Hamm, P.; Lim, M.; Hochstrasser, R. M. *J. Phys. Chem. B* **1998**, *102*, 6123.
(2) Asplund, M. C.; Zanni, M. T.; Hochstrasser, R. M. *Proc. Natl. Acad. Sci. U.S.A.* **2000**, *97*, 8219.
(3) Golonzka, O.; Khalil, M.; Demirdoven, N.; Tokmakoff, A. *Phys. Rev. Lett.* **2001**, *86*, 2154.
(4) Hamm, P.; Hochstrasser, R. M. Structure and dynamics of proteins and peptides: Femtosecond two-dimensional infrared spectroscopy. In *Ultrafast Infrared and Raman Spectroscopy*; Fayer, M. D., Ed.; Marcel Dekker: New York, 2001; Vol. 26, p 273.
(5) Ge, N.-H.; Zanni, M. T.; Hochstrasser, R. M. *J. Phys. Chem. A* **2002**, *106*, 962.
(6) Khalil, M.; Demirdoven, N.; Tokmakoff, A. *J. Phys. Chem. A* **2003**, *107*, 5258.
(7) Mukamel, S. *Annu. Rev. Phys. Chem.* **2000**, *51*, 691.
(8) Fang, C.; Wang, J.; Charnley, A. K.; Barber-Armstrong, W.; Smith, A. B.; Decatur, S. M.; Hochstrasser, R. M. *Chem. Phys. Lett.* **2003**, *382*, 586.
(9) Fang, C.; Wang, J.; Kim, Y. S.; Charnley, A. K.; Barber-Armstrong, W.; Smith, A. B., III; Decatur, S. M.; Hochstrasser, R. M. *J. Phys. Chem. B* **2004**, *108*, 10415.
(10) Rubtsov, I. V.; Wang, J.; Hochstrasser, R. M. *Proc. Natl. Acad. Sci. U.S.A.* **2003**, *100*, 5601.
(11) Kim, Y. S.; Wang, J.; Hochstrasser, R. M. *J. Phys. Chem. B* **2005**, *109*, 7511.
(12) Barron, L. D.; Hecht, L.; McColl, I. H.; Blanch, E. W. *Mol. Phys.* **2004**, *102*, 731.
(13) Nafie, L. A.; Freedman, T. B. Biological and pharmaceutical applications of vibrational optical activity. In *Infrared and Raman Spectroscopy of Biological Materials*; Gremlich, H.-U., Yan, B., Eds.; Marcel Dekker: New York, 2000; Vol. 24, p 15.
(14) Keiderling, T. A. *Curr. Opin. Chem. Biol.* **2002**, *6*, 682.
(15) Keiderling, T. A. Peptide and protein conformational studies with vibrational circular dichroism and related spectroscopies. In *Circular*

2D IR Spectra of Isotopomers of an α-Helix

J. Phys. Chem. B, Vol. 109, No. 39, 2005 **18663**

Dichroism: Principles and Applications, 2nd ed.; Berova, N., Nakanishi, K., Woody, R. W., Eds.; Wiley-VCH: New York, 2000; p 621.

(16) Fabian, H.; Chapman, D.; Mantsch, H. H. New trends in isotope-edited infrared spectroscopy. In *Infrared Spectroscopy of Biomolecules*; Mantsch, H. H., Chapman, D., Eds.; Wiley-Liss: Chichester, 1996; p 341.

(17) Wharton, C. W.; Page, M. G. P.; Chittock, R. S.; Regan, T. E.; Ward, S. *Laser Chem.* **1999**, *19*, 209.

(18) Zhang, M.; Fabian, H.; Mantsch, H. H.; Vogel, H. J. *Biochemistry* **1994**, *33*, 10883.

(19) Tadesse, L.; Nazarbaghi, R.; Walters, L. *J. Am. Chem. Soc.* **1991**, *113*, 7036.

(20) Paul, C.; Wang, J.; Wimley, W. C.; Hochstrasser, R. M.; Axelsen, P. H. *J. Am. Chem. Soc.* **2004**, *126*, 5843.

(21) Marsh, D. *J. Mol. Biol.* **2004**, *338*, 353.

(22) Starzyk, A.; Barber-Armstrong, W.; Sridharan, M.; Decatur, S. M. *Biochemistry* **2005**, *44*, 369.

(23) Barber-Armstrong, W.; Donaldson, T.; Wijesooriya, H.; Silva, R. A. G. D.; Decatur, S. M. *J. Am. Chem. Soc.* **2004**, *126*, 2339.

(24) Anderson, T. S.; Hellgeth, J.; Lansbury, P. T., Jr. *J. Am. Chem. Soc.* **1996**, *118*, 6540.

(25) Decatur, S. M.; Antonic, J. *J. Am. Chem. Soc.* **1999**, *121*, 11914.

(26) Patzlaff, J. S.; Zhang, J.; Brooker, R. J.; Barry, B. A. *Biochemistry* **2002**, *41*, 7366.

(27) Silva, R. A. G. D.; Kubelka, J.; Bour, P.; Decatur, S. M.; Keiderling, T. A. *Proc. Natl. Acad. Sci. U.S.A.* **2000**, *97*, 8318.

(28) Sachs, R. K.; Halverson, K. M.; Barry, B. A. *J. Biol. Chem.* **2003**, *278*, 44222.

(29) Torres, J.; Kukol, A.; Goodman, J. M.; Arkin, I. T. *Biopolymers* **2001**, *59*, 396.

(30) Mukherjee, P.; Krummel, A. T.; Fulmer, E. C.; Kass, I.; Arkin, I. T.; Zanni, M. T. *J. Chem. Phys.* **2004**, *120*, 10215.

(31) Diem, M. *Introduction to Modern Vibrational Spectroscopy*; Interscience: New York, 1993.

(32) Reisdorf, W. C., Jr.; Krimm, S. *Biochemistry* **1996**, *35*, 1383.

(33) Krimm, S.; Bandekar, J. *J. Adv. Protein Chem.* **1986**, *38*, 181.

(34) Jeffrey, G. A. *An Introduction to Hydrogen Bonding*; Oxford University Press: New York, 1997.

(35) Cho, M.; Yu, J.-Y.; Joo, T.; Nagasawa, Y.; Passino, S.; Fleming, G. R. *J. Phys. Chem.* **1996**, *100*, 11944.

(36) Lim, M.; Hamm, P.; Hochstrasser, R. M. *Proc. Natl. Acad. Sci. U.S.A.* **1998**, *95*, 15315.

(37) de Boeij, W. P.; Pshenichnikov, M. S.; Wiersma, D. A. *Chem. Phys. Lett.* **1996**, *253*, 53.

(38) Piryatinski, A.; Skinner, J. L. *J. Phys. Chem. B* **2002**, *106*, 8055.

(39) Ernst, R. R.; Bodenhausen, G.; Wokaun, A. *Principles of Nuclear Magnetic Resonance in One and Two Dimensions*; Oxford University Press: New York, 1987; Vol. 14.

(40) Torres, J.; Adams, P. D.; Arkin, I. T. *J. Mol. Biol.* **2000**, *300*, 677.

(41) Huang, R.; Kubelka, J.; Barber-Armstrong, W.; Silva, R. A. G. D.; Decatur, S. M.; Keiderling, T. A. *J. Am. Chem. Soc.* **2004**, *126*, 2346.

(42) Wang, J.; Hochstrasser, R. M. *Chem. Phys.* **2004**, *297*, 195.

(43) Torii, H.; Tasumi, M. *J. Chem. Phys.* **1992**, *96*, 3379.

(44) Kim, Y. S.; Hochstrasser, R. M. *J. Phys. Chem. B* **2005**, *109*, 6884.

(45) Mukamel, S. *Principles of Nonlinear Optical Spectroscopy*; Oxford University Press: New York, 1995; pp 212−213.

(46) Hamm, P.; Lim, M.; DeGrado, W. F.; Hochstrasser, R. M. *J. Phys. Chem. A* **1999**, *103*, 10049.

(47) Berman, H. M.; Westbrook, J.; Feng, Z.; Gilliland, G.; Bhat, T. N.; Weissig, H.; Shindyalov, I. N.; Bourne, P. E. *Nucleic Acids Res.* **2000**, *28*, 235.

(48) Baud, F.; Karlin, S. *Proc. Natl. Acad. Sci. U.S.A.* **1999**, *96*, 12494.

(49) Fisinger, S.; Serrano, L.; Lacroix, E. *Protein Sci.* **2001**, *10*, 809.

(50) Sicheri, F.; Yang, D. S. C. *Nature* **1995**, *375*, 427.

(51) Kobko, N.; Dannenberg, J. J. *J. Phys. Chem. A* **2003**, *107*, 6688.

(52) Estebanez-Perpina, E.; Bayes, A.; Vendrell, J.; Jongsma, M. A.; Bown, D. P.; Gatehouse, J. A.; Huber, R.; Bode, W.; Aviles, F. X.; Reverter, D. *J. Mol. Biol.* **2001**, *313*, 629.

(53) Shimamura, T.; Ibuka, A.; Fushinobu, S.; Wakagi, T.; Ishiguro, M.; Ishii, Y.; Matsuzawa, H. *J. Biol. Chem.* **2002**, *277*, 46601.

(54) Ghosh, T.; Garde, S.; Garcia, A. E. *Biophys. J.* **2003**, *85*, 3187.

(55) Garcia, A. E.; Sanbonmatsu, K. Y. *Proc. Natl. Acad. Sci. U.S.A.* **2002**, *99*, 2782.

(56) Vila, J. A.; Ripoll, D. R.; Scheraga, H. A. *Proc. Natl. Acad. Sci. U.S.A.* **2000**, *97*, 13075.